iScience

CellPress
OPEN ACCESS

Article

Demonstration of Enhanced Piezo-Catalysis for Hydrogen Generation and Water Treatment at the Ferroelectric Curie Temperature

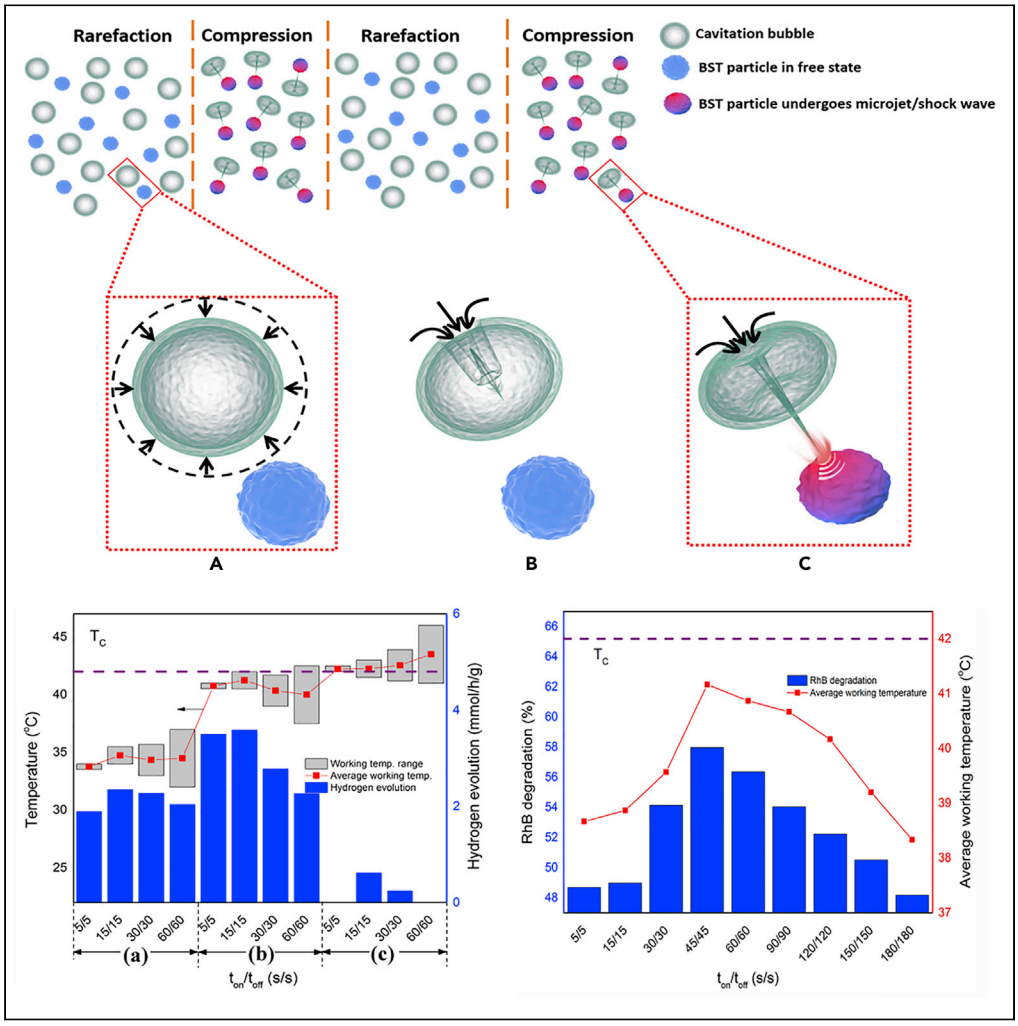

Pham Thi, Thuy Phuong, Yan, Zhang, Nick, Gathercole, ..., Kechao, Zhou, Steve, Dunn, Chris, Bowen

pttphuong@ict.vast.vn (P.T.T.P.)
yanzhang@csu.edu.cn (Y.Z.)
c.r.bowen@bath.ac.uk (C.B.)

HIGHLIGHTS

First demonstration of the positive impact of operating near T_c for piezo-catalysis

Ultrasound applied to achieve piezo-catalysis near T_c

High hydrogen production rate and degradation rate were achieved at the T_c

Piezo-catalysis is a new avenue for low T_c and lead-free ferroelectrics

Thuy Phuong et al., iScience *23*, 101095
May 22, 2020
https://doi.org/10.1016/j.isci.2020.101095

iScience

CellPress
OPEN ACCESS

Article

Demonstration of Enhanced Piezo-Catalysis for Hydrogen Generation and Water Treatment at the Ferroelectric Curie Temperature

Pham Thi, Thuy Phuong,[2,5,*] Yan, Zhang,[1,5,*] Nick, Gathercole,[3] Hamideh, Khanbareh,[3] Nguyen Phuc, Hoang Duy,[2] Xuefan, Zhou,[1] Dou, Zhang,[1] Kechao, Zhou,[1] Steve, Dunn,[4] and Chris, Bowen[3,6,*]

SUMMARY

Hydrogen can contribute significantly to the energy mix of the near future, as it is an attractive replacement for fossil fuels due to its high energy density and low greenhouse gas emission. A fascinating approach is to use the polarization change of a ferroelectric due to an applied stress or temperature change to achieve piezo- or pyro-catalysis for both H_2 generation and wastewater treatment. We exploit low Curie temperature (T_c) ferroelectrics for polarization-driven electrochemical reactions, where the large changes in polarization and high activity of a ferroelectric near its T_c provides a novel avenue for such materials. We present experimental evidence for enhanced water splitting and rhodamine B degradation via piezo-catalysis by ultrasonic excitation at its T_c. Such work provides an effective strategy for water splitting/treatment systems that employ low T_c ferroelectrics under the action of mechanical stress or/and thermal fluctuations.

INTRODUCTION

Hydrogen is considered as a promising and abundantly available renewable fuel with a high energy density per unit mass, with potential to act as a carbon-free energy carrier in response to the global energy crisis and need to reduce environmental pollution (Xiang et al., 2016; Zhu et al., 2018). The ability to couple piezoelectric and pyroelectric effects with electrochemical processes continues to attract attention to exploit mechanical vibrations and temperature fluctuations for hydrogen generation, water treatment, photocatalysis, and materials processing (Zhang et al., 2015, 2017; Ismail et al., 2019; Mushtaq et al., 2018). Starr et al. (Starr et al., 2012; Starr and Wang, 2013, 2015) provided a detailed overview of the fundamentals of piezocatalysis and examined the surface electrochemistry of a piezoelectric whose polarization changed in response to a mechanical strain. To demonstrate its potential, hydrogen generation was achieved by oscillating a piezoelectric $Pb(Mg_{1/3}Nb_{2/3})O_3$-32$PbTiO_3$ (PMN-PT) cantilever in contact with deionized water (Starr and Wang, 2013). Piezoelectric materials that have been examined include zinc oxide, which have been combined with photocatalytic studies by the application of both ultrasound and light (Xue et al., 2015; Tan et al., 2015; Ma et al., 2019; Hong et al., 2016), or heat to explore pyroelectric effects due to a change in polarization with temperature (Qian et al., 2017; Tang et al., 2018). Single- and few-layer piezoelectric materials, such as MoS_2 and $MoSe_2$, have also been examined in detail by Wu *et al.* (Wu et al., 2016b, 2017, 2018c; Lin et al., 2017).

Recent work by Kakekhani et al. (Kakekhani and Ismail-Beigi, 2015, 2016a, 2016b; Kakekhani et al., 2016) has focused on the use of ferroelectric materials for polarization-driven catalysis, which exhibit both piezo- and pyroelectricity. These materials are of interest because their polarization direction can be changed, thereby enabling a switching of surface chemistry. Modeling work, based on $PbTiO_3$, showed that splitting of water into oxygen and hydrogen is possible by thermally cycling a ferroelectric above and below its Curie temperature (T_c) when in contact with water. Initial experimental effort to demonstrate this process used pyroelectrics as an external charge source to generate a potential difference for water splitting (Zhang et al., 2019; Xie et al., 2017). However, recent work has shown that it is possible to generate hydrogen by simply placing ferroelectric particles in direct contact with water and subjecting them to cyclic heating and cooling (Belitz et al., 2017; Xu et al., 2018b; You et al., 2018a). As a model ferroelectric material, barium titanate has often been explored for tribo- (Li et al., 2019), piezo- (Belitz et al., 2017; Feng et al., 2019; Hong et al., 2010,

[1]State Key Laboratory of Powder Metallurgy, Central South University, Changsha, Hunan, 410083, China

[2]Institute of Chemical Technology, Viet Nam Academy of Science and Technology, Ho Chi Minh, Vietnam

[3]Department of Mechanical Engineering, University of Bath, Bath BA2 7AY, UK

[4]Chemical Engineering, School of Engineering, London South Bank University, 103 Borough Road, London SE1 0AA, UK

[5]These authors contributed equally

[6]Lead Contact

*Correspondence: pttphuong@ict.vast.vn (P.T.T.P.), yanzhang@csu.edu.cn (Y.Z.), c.r.bowen@bath.ac.uk (C.B.)

https://doi.org/10.1016/j.isci.2020.101095

2012; Jin et al., 2019; Pan et al., 2019; Wu et al., 2018a), and pyroelectric catalysis (Benke et al., 2015; Wu et al., 2018b; Xia et al., 2017). This is primarily due to its lead-free nature, low-cost, and ease of manufacture in a wide variety of forms, such as nanofibers (Wu et al., 2018a; Xia et al., 2017), composites (Min et al., 2018), and particles (Belitz et al., 2017), which can be decorated with semiconductors (Liu et al., 2019) to enhance catalytic performance.

The working temperature of a ferroelectric, in relation to its Curie temperature, is likely to strongly influence any polarization-driven catalysis because the piezoelectric, pyroelectric (Zhang et al., 2020), dielectric, and electrocaloric properties are often maximized near the Curie temperature due to (1) intrinsic effects as a result of the large changes in polarization with stress or temperature or (2) the enhanced extrinsic contributions associated with domain wall motion (Karthik and Martin, 2011). However, it is surprising that there has been little effort to date that examines this experimentally. Evidence of a ferroelectric enhancement in a photochemical environment has been reported (Cui et al., 2013, 2019), where the photocatalytic degradation of a dye molecule was enhanced below the T_c due to an enhanced carrier lifetime (Morris et al., 2016).

Although barium titanate has been widely explored for polarization-driven catalysis, its Curie temperature is above the boiling point of water ($T_c \sim 120°C$ (Harwood et al., 1947)), thereby making an evaluation of catalytic performance in water above and below T_c impossible. Other high Curie temperature ferroelectrics studied to date with a $T_c > 100°C$ include $LiNbO_3$ (Gutmann et al., 2012), $LiTaO_3$ (Gutmann et al., 2012), $PbZr_xTi_{1-x}O_3$ (Lin et al., 2014; Feng et al., 2017), $BiFeO_3$ (Liu and Wu, 2019; Wu et al., 2016a; You et al., 2019), $NaNbO_3$ (You et al., 2018b; Wang et al., 2019) ($T_c \sim 350°C$ (Guo et al., 2015)), $ZnSnO_3$ (Wang and Wu, 2020), and $KNbO_3$ (Jia et al., 2019) ($T_c \sim 434°C$ (Matthias and Remeika, 1951)), where piezo-catalytic hydrogen generation and degradation of water contaminants has been achieved at temperatures that are well below T_c. One low Curie temperature material ($T_c < 100°C$) that has been studied is barium strontium titanate (Xu et al., 2018a, 2018b), although the influence of operating temperature on piezo- or pyro-catalytic performance has yet to be been examined.

In this paper we provide the first examination of the influence of working temperature, in relation to the T_c, on the *piezo-catalytic* performance for hydrogen generation and degradation of water contaminants (rhodamine B [RhB]) under the application of ultrasound. We have selected a $BaTiO_3$-based solid solution based on $Ba_{0.75}Sr_{0.25}TiO_3$ due to its relatively low Curie temperature ($T_c \sim 42°C$), which allows us to systematically examine piezo-catalysis at temperatures (1) below T_c, (2) at the T_c, and (3) above T_c. Additional advantages include its lead-free composition, low cost, and comparable ferroelectric, piezo-, and pyroelectric performance with respect to lead-based piezoelectric ceramics (Wu, 2018; Airimioaei et al., 2017).

RESULTS AND DISCUSSION

Although the initial pioneering work of Starr et al. (Starr and Wang, 2013) used a simple cantilever configuration to generate a strain in the piezoelectric, a number of researchers have used ultrasound to apply a mechanical deformation. A difference between these two approaches is that the application of ultrasound can lead to the formation of bubbles by cavitation of water, whose subsequent violent collapse can create localized hotspots and high pressures to generate temperatures of ~5000°C and pressures of ~500 atm. Such cavitation events have also been shown to generate hydrogen from water (Islam et al., 2019), termed *sono-chemical* generation in this paper. As a result, close control of operating temperature during the application of ultrasound was undertaken in this work, along with the use of control samples that contained non-ferroelectric ceramic particles (termed *control*) or were particulate free (termed *blank*) to separate the sono-chemical and piezo-catalytic effects, a factor that is often ignored. By careful experimental design, the results presented here therefore provide new insights into the influence of operating temperature, in relation to the T_c, on piezo-catalytic performance and demonstrates the importance of selecting an optimum operating temperature or T_c for improved water splitting or water treatment; it also demonstrates that harnessing the inherent polarization changes in ferroelectrics with stress and temperature can aid chemical conversion.

In terms of the ferroelectric $Ba_xSr_{1-x}TiO_3$ (BST) material used for this study, Figure 1A shows the XRD data of the synthesized powders with Miller indices indicated in the 2θ range of 20–90°, where the sharp and well-defined XRD peaks indicate its high crystallinity. Only one crystalline (inset of Figure 1A) phase was detected, with no presence of secondary phase. By comparing XRD data with standard JCPDS no. 44-0093, the synthesized powders had the same characteristic peaks as tetragonal perovskite BST.

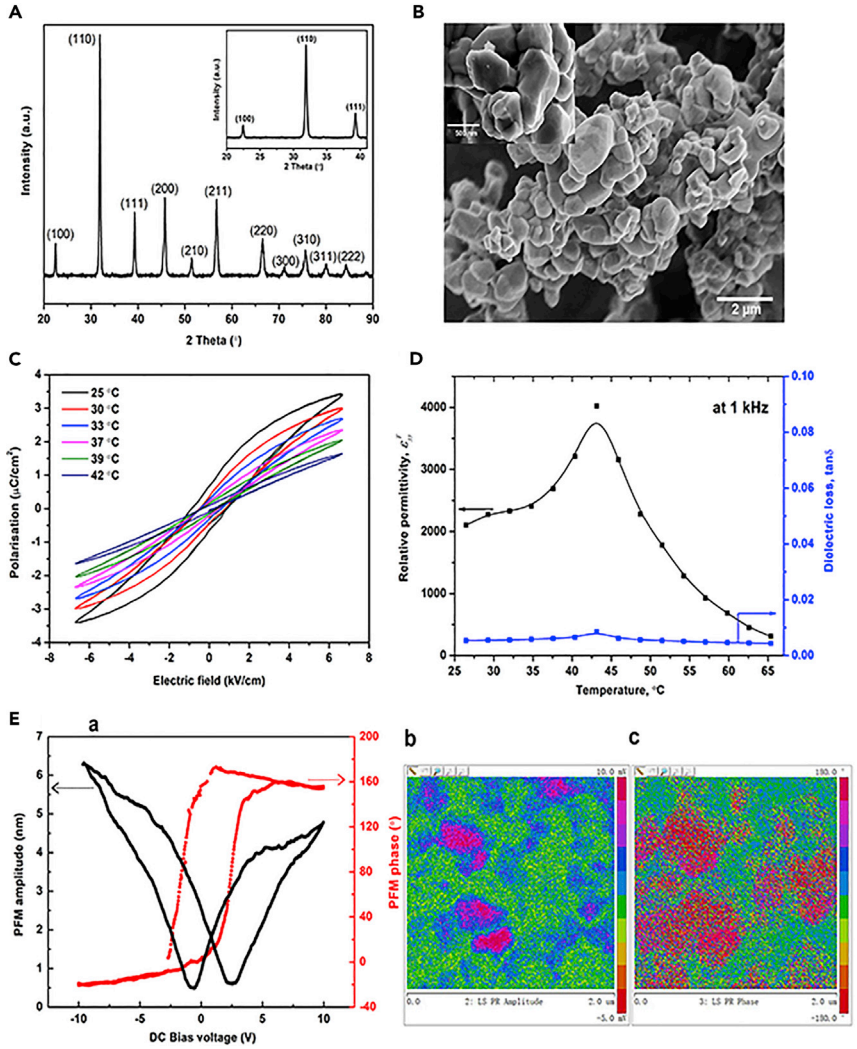

Figure 1. X-ray Diffraction (XRD) Patterns, Microstructural Morphology, Dielectric and Ferroelectric Properties of Synthesized BST

(A) XRD patterns of the synthesized powder. (B) SEM image of the synthesized BST powder, inset shows a higher magnification. (C) polarization-electric field (*P-E*) loops of sintered BST as a function of temperature and electric field. (D) relative permittivity and dielectric loss of the sintered BST dense pellet as a function of temperature at a frequency of 1 kHz. (E) local ferroelectric domain switching. (a) Local hysteresis loop behavior for the amplitude and phase, (b) PFM amplitude, (c) PFM phase.

Figure 1B shows a scanning electron microscopy (SEM) image of the BST particles, where it can be seen that the particles prepared by the solid-state reaction with an equi-axed morphology exhibited a particle size of 0.2–1.2 μm. Figure 1C shows the ferroelectric polarization–electric field (*P-E*) hysteresis loops of a sintered BST pellet with the relative density of 98.9% at different temperatures ranging from 25 to 42°C; a sintered sample was simply used to facilitate characterization of the *P-E* although powders will be used for piezo-catalysis. At room temperature, the saturated polarization and coercive field were ~3.5 μC cm^{-2} and ~1 kV cm^{-1}, respectively. With an increase of temperature, the polarization decreased and the hysteresis loops became slimmer and the hysteresis loop exhibited an almost linear response at 42°C, which can be regarded as the Curie temperature, similar to Ashish's observation (Pradeep et al., 2010). This is also in accordance with the dielectric properties illustrated in Figure 1D, where the relative permittivity (ε) is found to initially increase with temperature, and then reaches a maximum at the Curie temperature of T_c ~ 42°C, and is then followed by a decrease in permittivity with increasing temperature that can be assigned to the transition from the asymmetric tetragonal (ferroelectric) to symmetric cubic (paraelectric) phase. The

dielectric loss (loss tangent) exhibited a similar trend but remained low in the temperature range of 26.5–65.5°C. The AC conductivity (σ) increased with frequency f, based on the equation of $\sigma = 2\pi f\varepsilon$, and there is only a limited change in AC conductivity in temperature range of 25–42°C, as shown in Figure S1. Figure 1E shows the domain pattern and the local surface displacement via piezo-force microscopy (PFM) as a function of the DC bias voltage from −10 V to 10 V. As shown in Figure 1E-a, a well-defined hysteresis response of the BST sample can be observed locally, further confirming the ferroelectricity in BST ceramic below its Curie temperature. The local surface displacement due to the converse piezoelectric effect is shown in Figure 1E-b, indicating the magnitude of the piezoelectric coefficient along the normal direction with a mean d33* of ∼430 pm V^{-1}, calculated from the PFM amplitude. An approximately 180° phase difference (from ∼−20° to ∼160°) can be found in Figure 1E-a, together with two different color contrasts with an ∼180° phase difference, shown in Figure 1E-c, indicating the switching nature of the domains in the BST material. In summary, the material is clearly ferroelectric and exhibits a low Curie temperature of $T_c \sim 42$°C, which makes BST a suitable candidate for the investigation of the effect of working temperature on piezoelectrically enhanced water splitting.

We now examine the influence of working temperature on the water splitting capability of BST, where the experimental setup is outlined in Figures S2 and S3. The apparatus was used to apply ultrasound to BST powder dispersed in a mixture of water and methanol, which was used as a sacrificial reagent to scavenge OH radicals (Penconi et al., 2015). As can be seen in the Figure S4, the application of ultrasound at a fixed power level and frequency (40 kHz) leads to an increase in temperature of the bulk solution with excitation time. Because sono-chemical hydrogen production can be affected by ultrasonic frequency, dissolved gas, acoustic power, and liquid temperature (Rashwan et al., 2019), they were closely controlled to ensure a stable sono-chemical hydrogen generation, as in Figure S4, to enable analysis of the effect of working temperature on piezo-catalytic hydrogen production. To select a specific working temperature, without altering other conditions, the hydrogen production rates at the same ultrasound *on*/*off* time ratio (1/1) with different interval times were determined using initial water bath temperatures of 23, 30, and 33°C. This ensured that the ultrasound was applied in a narrow working temperature range in relation to the T_c of the material. In order to separate the amount of hydrogen that was generated by the ultrasound *on* and *off* processes, the product gases during *on* and *off* time periods were continuously swept by an argon stream and sent directly to the gas chromatography for immediate hydrogen measurement, as in Figure S2. When the ultrasound *off* time was greater than the retention time of the gases in the system, any hydrogen produced was fully swept out of the measurement system; when the *off* time is shorter than the retention time background hydrogen is detected due to accumulated hydrogen in the system. Measurement uncertainties have been estimated by at least three experiments.

Figure 2A shows the working temperature and average piezo-catalytic hydrogen generation obtained with different ultrasound on/off time ratios at different water bath temperatures. It can be seen that the degree of hydrogen evolution increases as the working temperature approaches the T_c of the material; however, when the working temperature exceeds the T_c the degree of hydrogen evolution decreases because the BST is no longer ferroelectric. In addition, the highest and most distinct hydrogen evolution was obtained at temperatures of 40–42°C, near the T_c, where the material exhibits the highest and most distinct piezoelectric coefficient. This can be explained by examination of Figure 2B (Justin Raj et al., 2011; Whatmore, 2017), which shows a schematic of the temperature dependence of spontaneous polarization of BST and its dependence with stress (piezo-coefficient). At low temperatures, below the T_c, the piezo-coefficients of the ferroelectric tetragonal phase are relatively small, due to the relatively small changes in polarization in response to a stress. As the temperature approaches T_c, greater changes in polarization are expected with an applied stress change and the piezo-coefficients increase, leading to an increase in piezo-catalytic performance due to the application of ultrasound. Above the T_c the material changes to the paraelectric cubic phase and exhibits no change in polarization with ultrasound.

Figure 2C shows that use of inert α-Al_2O_3 (as a non-ferroelectric control) did not alter the hydrogen evolution, whereas the addition of ferroelectric BST resulted in a large difference compared with both "control" (α-Al_2O_3) and "blank" (no addition of any solid substances) tests. In addition, further evidence of no enhancement in hydrogen production at a working temperature that exceeds the T_c is seen in Figure 2D, indicating that a loss in the polarization of the material (see Figures 1C and 1D) correlates with a reduction in hydrogen production. Clearly, there is a strong link between the temperature change, working temperature, and the hydrogen production in the presence of BST, whereas the control and blank test is not

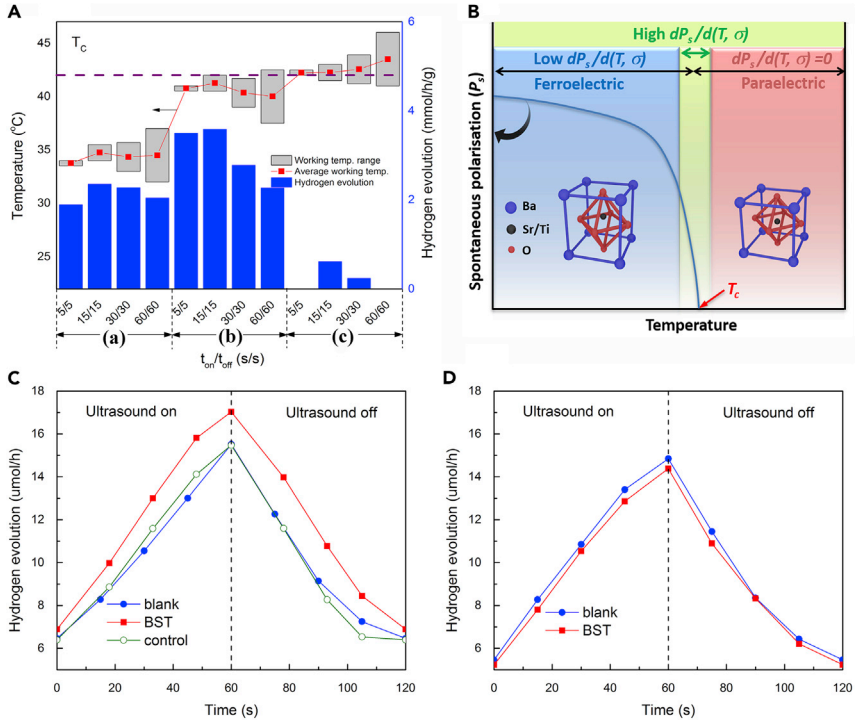

Figure 2. Hydrogen Evaluation under Different Water Bath Temperatures

(A) Working temperature and average piezo-catalytic hydrogen generation obtained with different ultrasound on/off time ratios (t_{on}/t_{off}) at different water bath temperature (T_{bath}), where (A), (B), and (C) relate to water bath temperatures of 23, 30, and 33°C respectively. (B) Effect of T_c on polarization. Total hydrogen evolution during one cycle of ultrasound excitation at different bulk solution temperature, (C) ~ 40°C and (D) ~ 43°C. Measurement uncertainties have been estimated by at least three experiments.

influenced, confirming again the piezo-catalytic activity of BST. The dispersion of BST particles in an aqueous solution and powder microstructure morphology after ultrasound excitation are shown in Figure S5, which indicate the well-dispersed state of BST particles in the solution and no significant change in morphology due the application of ultrasound. The fact that the efficiency of the chemical reaction was reduced when the working temperature was higher than the T_c indicates that any increased thermal motion of the dispersed powder due to the increased temperature was not the primary reason for the improved catalytic performance (Mushtaq et al., 2019).

Figure 3 shows the proposed mechanism of the generation of surface charge induced by the application of ultrasound and generation of cavitation bubbles. In an ultrasonic bath, cavitation bubbles (Haar, 2015) can be formed as a result of the high-intensity ultrasound, where the cavitation bubbles expand during the rarefaction and collapse in the compression of the sound wave; see also Figure S6. A shock wave or microjet is produced from the collapsed bubbles, which leads to a high temperature and pressure (Kenneth andSuslick, 1998) with intense local heating of 5000 K, large pressures of 500 atm, heating/cooling rates of > 10^9 K sec^{-1}, and liquid jet streams of 360 km h^{-1} (Suslick, 1990). However, in the presence of small collapsed water bubbles, typically 10–20 μm in size (Xu et al., 2015), the temperature of BST particles are likely to rapidly fall to the working temperature of the water bath and monitored in real time. Therefore, it is believed that the BST particles in the ultrasonic bath can be subjected to a compressive load (σ) normal or perpendicular to the polarization direction of a ferroelectric domain, which can act to change the polarization of the BST particles, and this has a greater effect near the T_c. It is of interest to consider the differences in the generated voltage and charge as the temperature increases up to the Curie temperature. The voltage (V) is determined by the piezoelectric voltage coefficient, $g_{ij} = d_{ij}/\varepsilon$, and is a measure of electric field per unit stress; the g_{ij} coefficient decreases with temperature as a result of an increase in permittivity. The level of charge (Q) is determined by the piezoelectric charge coefficient, d_{ij}, which reaches a maximum at its T_c (Miclea et al., 2007; Chen et al., 2014). Based on Faraday's law, $m = QM/Fz$, where m is the mass of H_2, Q is the total

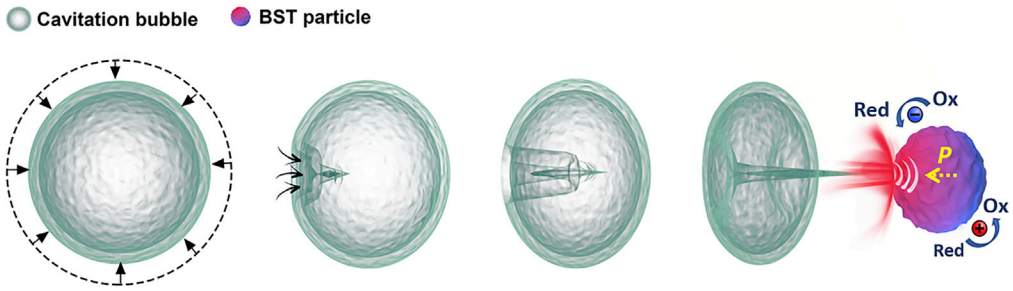

Figure 3. Schematic of the Effect of Cavitation on a BST Ferroelectric Particle under the Application of Ultrasound

The compressive shock wave acts to reduce the level of polarization, leading to the formation of surface charges for electrochemical reaction, such as H_2 generation.

electric charge, $F = 96.485$ C mol^{-1} is the Faraday constant, M is the molar mass of the substance, and z is the valence number of ions of the substance; the amount of H_2 and RhB degradation product depend on the charge generated, whereas the threshold voltage is the driving force for the chemical reactions. The large change of polarization with stress and high d_{ij} near the T_c is therefore beneficial to increase the quantity of charge and H_2 generated. The overall mechanism generates a positive and negative charge on opposing surfaces (Equation 1) (Xu et al., 2018b).

$$(\sigma)$$

$$BST \rightarrow BST + q^- + q^+ \qquad \text{(Equation 1)}$$

The positive pyroelectric charges ($q+$) are able to oxidize water molecules at the surface of the BST particle, thereby producing H^+ and O_2 (Equation 2):

$$2q^+ + H_2O \rightarrow 2H^+ + {}^1/_2O_2 \qquad \text{(Equation 2)}$$

The H^+ can react with the negative pyroelectric charges (q^-) to create hydrogen (Equation 3).

$$2H^+ + 2q^- \rightarrow H_2 \qquad \text{(Equation 3)}$$

Above the T_c the polarization is lost and no pyroelectric charges are produced (Equation 1) and the piezo-catalytic activity is therefore reduced, as in Figures 2A and 2D.

Figure 4 and Table S1 provide a summary of the hydrogen evolution rates using different methods reported in the literature. It is clear that by optimization of the working temperature in relation to the T_c a promising piezo-catalytic hydrogen production rate of 3.59 mmol/g/h is achieved, which is much larger than those obtained from a simple pyro-catalytic effect from BST (7.8 μmol/g/h) (Xu et al., 2018b) and from other piezoelectric materials (Wang and Wu, 2020; You et al., 2019; Su et al., 2018), with a Curie temperature of 32°C ($Ba_{0.7}Sr_{0.3}TiO_3$) (Xu et al., 2018b), 820°C ($BiFeO_3$) (Kiselevet al., 1963), 622°C (MoS_2) (Xia et al., 2016), and >700°C ($ZnSnO_3$) (Zhang et al., 2010). The production rate also remained stable for a testing period of up to 700min, see Figure S7.

A similar sensitivity of performance in relation to T_c is also observed in the case of sono-piezo-catalytic degradation of RhB, as can be seen in Figure 5A. The highest working temperature was observed in the case of ultrasound with a 45 s on/off interval, 41°C, respectively, exhibiting the highest RhB degradation of 58%. The degradation rate of RhB then decreased with an increase in the time interval due to decrease in working temperature. Figure 5B shows that the characteristic adsorption peak of RhB gradually decreased with increasing reaction time and complete degradation of the RhB could be achieved after 120 min. From the above results, it can be concluded that approaching T_c is the most important strategy that should be considered for maximizing the pyro-catalytic effect. Figure 5C illustrates the kinetics of the RhB degradation, where a linear relationship between $\ln(C_0/C_t)$ and irradiation time for the degradation

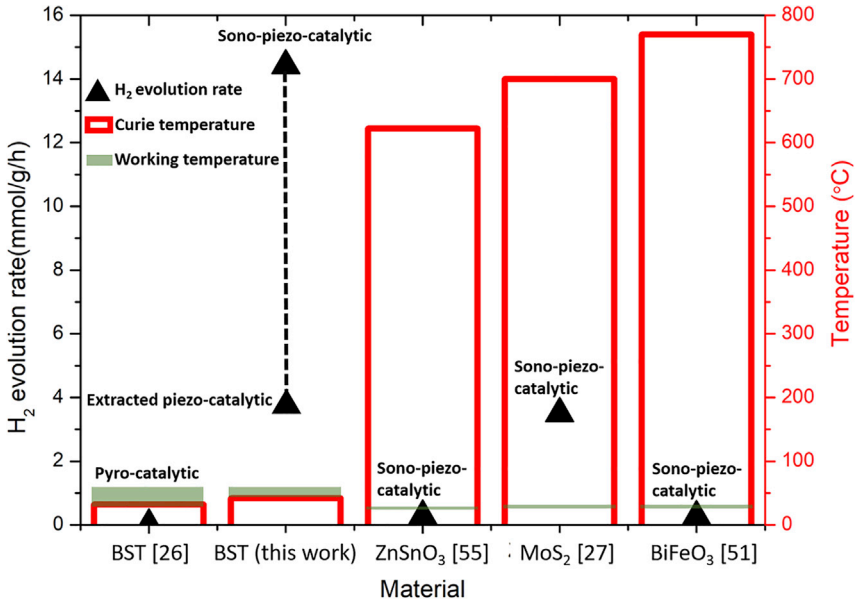

Figure 4. Comparisons of Hydrogen Evolution Rate under Different Conditions

of RhB can be fitted to $\ln(C_0/C_t) = kt$, where C_0 and C_t are the RhB concentration at time t_0 and t respectively, and k is the apparent first-order rate constant (min^{-1}). The slope of the straight line represents the kinetic constant k with a calculated value of 0.0245 min^{-1} and R^2 of 0.9967, implying a good catalytic activity that is comparable to that of commercial Degussa P25 for sono-catalytic degradation of RhB (Zhou et al., 2015).

Conclusion

In summary we have provided the first experimental demonstration of the importance of working temperature, in relation to the Curie temperature for piezo-catalytic hydrogen generation and degradation of water contaminants (RhB) under ultrasound. The piezo-catalytic performance of the ferroelectric materials increases significantly near the T_c due to an increase in piezo-coefficients and the impact of cavitation of the local stress; further work to examine any potential pyroelectric contributions due to the rapid localized temperature changes at cavitation sites would be of interest. A wide variety of lead-free ferroelectrics are currently under investigation (Zheng et al., 2018), and although the low T_c of particular systems makes them inappropriate for conventional sensor or actuator applications, they would be of interest for such piezo-catalysis. Under optimum conditions of operation near T_c the addition methanol at only 4% can enhance the hydrogen evolution with negligible generation of other impurities. Consequently, a high hydrogen production rate of 10.83 μmol/h was achieved, which is much higher than previously reported, such as 3.4 μmol/h by Wang et al. (Wang et al., 2010) (see Table S1). We also demonstrate the need for careful control of experiments to separate both sono-chemical and pyro-chemical effects. It is also of interest to explore other modes of operation such as piezo-photo-catalytic effects (Tan et al., 2015; Huang et al., 2017) near T_c or mixing ferroelectric particles of different T_c to enable operation over a range of temperatures. Of particular interest here is that for the materials selected for this study, $Ba_xSr_{1-x}TiO_3$, the Curie temperature can be tailored from −200°C to 120°C (Airimioaei et al., 2017; Mbarki et al., 2014) and provides ample opportunities to tune the Curie temperature for a range of working temperatures for optimum piezo- and pyro-catalysis.

Limitations of the Study

Particles of ferroelectric were suspended in water in this work, and methods to disperse larger amounts of particulates in water are needed to improve the amount hydrogen formed or allow scale-up for water treatment. Potential avenues of research could include porous materials. Although ultrasound was used in this work, harvesting ambient sources of energy would be beneficial; this could include inducing cavitation from water flow or using temperature fluctuations.

METHODS

All methods can be found in the accompanying Transparent Methods supplemental file.

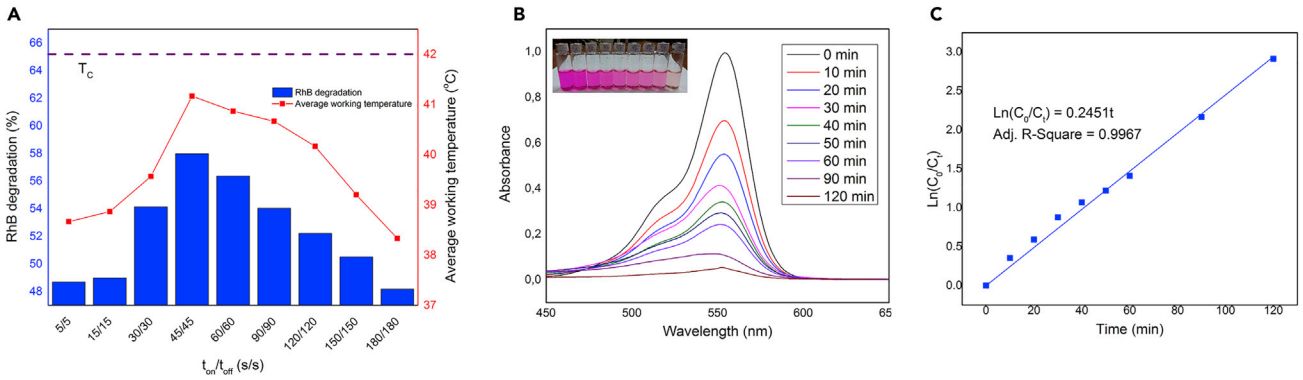

Figure 5. RhB Degradation Performance under Different Water Bath Temperatures

(A) Average working temperature and RhB degradation obtained after 30 min of excitation time with different ultrasound *on*/*off* time ratios. (B) Absorbance spectra of RhB solution after different treated time at average working temperature of 41°C with *on*/*off* ratio of 45s/45s in the presence of BST. (C) Kinetic plot of $ln(C_0/C_t)$ vs irradiation time for RhB degradation.

DATA AND CODE AVAILABILITY

The datasets generated during and/or analyzed during the current study are available from the corresponding author on reasonable request.

SUPPLEMENTAL INFORMATION

Supplemental Information can be found online at https://doi.org/10.1016/j.isci.2020.101095.

ACKNOWLEDGMENTS

We acknowledge the Academy of Medical Sciences GCRF fund (GCRFNGR2 -10059), ERC project (ERC-2017-PoC-ERC-Proof of Concept, grant no. 789863) and The Leverhulme Trust (RGP-2018-290) for their support. Y.Z. also would like to acknowledge the support from State Key Laboratory of Powder Metallurgy, Central South University, Changsha, China.

AUTHOR CONTRIBUTIONS

Conceptualization, P.T.T.P., Y.Z., S.D., and C.R.B.; Investigation, P.T.T.P., Y.Z., N.G., N.P.H.D., X.Z., D.Z., K.Z., and C.R.B.; Writing—Original Draft, P.T.T.P., Y.Z., and C.R.B.; Writing—Review & Editing, P.T.T.P., Y.Z., H.K., S.D., and C.R.B.; Funding Acquisition, P.T.T.P., Y.Z., and C.R.B.

DECLARATION OF INTERESTS

The authors declare no competing interests.

Received: February 23, 2020
Revised: April 10, 2020
Accepted: April 17, 2020
Published: May 22, 2020

REFERENCES

Airimioaei, M., Buscaglia, M.T., Tredici, I., Anselmi-Tamburini, U., Ciomaga, C.E., Curecheriu, L., Bencan, A., Buscaglia, V., and Mitoseriu, L. (2017). $SrTiO_3$–$BaTiO_3$nanocomposites with temperature independent permittivity and linear tunability fabricated using field-assisted sintering from chemically synthesized powders. J. Mater. Chem. C *5*, 9028–9036.

Belitz, R., Meisner, P., Coeler, M., Wunderwald, U., Friedrich, J., Zosel, J., Schelter, M., Jachalke, S., and Mehner, E. (2017). Waste Heat Energy Harvesting by Use of BaTiO3 for Pyroelectric Hydrogen Generation (Energy Harvesting and Systems).

Benke, A., Mehner, E., Rosenkranz, M., Dmitrieva, E., Leisegang, T., St Cker, H., Pompe, W., and Meyer, D.C. (2015). Pyroelectrically driven ●OH generation by barium titanate and palladium nanoparticles. J. Phys. Chem. C *119*, 18278–18286.

Chen, J., Cheng, J., and Dong, S. (2014). Review on high temperature piezoelectric ceramics and actuators based on $BiScO_3$–$PbTiO_3$ solid solutions. J. Adv. Dielectrics *04*, 1430002.

Cui, Y., Briscoe, J., and Dunn, S. (2013). Effect of ferroelectricity on solar-light-driven photocatalytic activity of $BaTiO_3$—influence on the carrier separation and stern layer formation. Chem. Mater. *25*, 4215–4223.

Cui, Y., Sun, H., Briscoe, J., Wilson, R., Tarakina, N., Dunn, S., and Pu, Y. (2019). Influence of ferroelectric dipole on the photocatalytic activity

of heterostructured BaTiO3/a-Fe_2O_3. Nanotechnology *30*, 255702.

Feng, Y., Ling, L., Wang, Y., Xu, Z., Cao, F., Li, H., and Bian, Z. (2017). Engineering spherical lead zirconatetitanate to explore the essence of piezo-catalysis. Nano Energy *40*, 481–486.

Feng, J., Sun, J., Liu, X., Zhu, J., Xiong, Y., and Tian, S. (2019). Enhancement and mechanism of nano-$BaTiO_3$piezocatalytic degradation of tricyclazole by co-loading Pt and RuO2. Environ. Sci. Nano *6*, 2241–2252.

Guo, H., Shimizu, H., and Randall, C.A. (2015). Direct evidence of an incommensurate phase in NaNbO3 and its implication in $NaNbO_3$-based lead-free antiferroelectrics. Appl. Phys. Lett. *107*, 112904.

Gutmann, E., Benke, A., Gerth, K., B Ttcher, H., Mehner, E., Klein, C., Krause-Buchholz, U., Bergmann, U., Pompe, W., and Meyer, D.C. (2012). Pyroelectrocatalyticdisinfection using the pyroelectric effect of nano- and microcrystalline $LiNbO_3$ and $LiTaO_3$ particles. J. Phys. Chem. C *116*, 5383–5393.

Haar, M.W.F.T. (2015). Cavitation in Biomedicine (Springer).

Harwood, M.G., Popper, P., and Rushman, D.F. (1947). Curie point of barium titanate. Nature *160*, 58–59.

Hong, K.-S., Xu, H., Konishi, H., and Li, X. (2010). Direct water splitting through vibrating piezoelectric microfibers in water. J. Phys. Chem. Lett. *1*, 997–1002.

Hong, K.-S., Xu, H., Konishi, H., and Li, X. (2012). Piezoelectrochemical effect: a new mechanism for azo dye decolorization in aqueous solution through vibrating piezoelectric microfibers. J. Phys. Chem. C *116*, 13045–13051.

Hong, D., Zang, W., Guo, X., Fu, Y., He, H., Sun, J., Xing, L., Liu, B., and Xue, X. (2016). High piezo-photocatalytic efficiency of CuS/ZnO nanowires using both solar and mechanical energy for degrading organic dye. ACS Appl. Mater. Interfaces *8*, 21302–21314.

Huang, H., TU, S., Zeng, C., Zhang, T., Reshak, A.H., and Zhang, Y. (2017). Macroscopic polarization enhancement promoting photo- and piezoelectric-induced charge separation and molecular oxygen activation. Angew. Chem. Int. Ed. *56*, 11860–11864.

Islam, M.H., Burheim, O.S., and Pollet, B.G. (2019). Sonochemical and sonoelectrochemical production of hydrogen. Ultrason.Sonochem. *51*, 533–555.

Ismail, M., Wu, Z., Zhang, L., Ma, J., Jia, Y., Hu, Y., and Wang, Y. (2019). High-efficient synergy of piezocatalysis and photocatalysis in bismuth oxychloride nanomaterial for dye decomposition. Chemosphere *228*, 212–218.

Jia, S., Su, Y., Zhang, B., Zhao, Z., Li, S., Zhang, Y., Li, P., Xu, M., and Ren, R. (2019). Few-layer MoS_2nanosheet-coated KNbO3 nanowire heterostructures: piezo-photocatalytic effect enhanced hydrogen production and organic pollutant degradation. Nanoscale *11*, 7690–7700.

Jin, C., Liu, D., Hu, J., Wang, Y., Zhang, Q., Lv, L., and Zhuge, F. (2019). The role of microstructure in piezocatalytic degradation of organic dye pollutants in wastewater. Nano Energy *59*, 372–379.

Justin Raj, C., Kundu, S., and Varma, K.B.R. (2011). Investigation of dielectric, piezoelectric and ferroelectric properties of b-axis grown triglycinesulphate single crystal. Appl. Phys. A *105*, 1025–1031.

Kakekhani, A., and Ismail-Beigi, S. (2015). Ferroelectric-based catalysis: switchable surface chemistry. ACS Catal. *5*, 4537–4545.

Kakekhani, A., and Ismail-Beigi, S. (2016a). Ferroelectric oxide surface chemistry: water splitting via pyroelectricity. J. Mater. Chem. A *4*, 5235–5246.

Kakekhani, A., and Ismail-Beigi, S. (2016b). Polarization-driven catalysis via ferroelectric oxide surfaces. Phys. Chem. Chem. Phys. *18*, 19676–19695.

Kakekhani, A., Ismail-Beigi, S., and Altman, E.I. (2016). Ferroelectrics: a pathway to switchable surface chemistry and catalysis. Surf. Sci. *650*, 302–316.

Karthik, J., and Martin, L.W. (2011). Pyroelectric properties of polydomain epitaxial $Pb(Zr_{1-x}Ti_x)O_3$ thin films. Phys. Rev. B *84*, 024102.

Kenneth, S., and Suslick, K.-O. (1998). Encryclopedia of Chemical Technology, Inc (John Wiley & Sons).

Kiselev, S.V., Ozerov, R.P., and Zhdanov, G.S. (1963). Detection of magnetic order in ferroelectric $BiFeO_3$ by neutron diffraction. Soviet Phys. Doklady *7*, 742–744.

Li, P., Wu, J., Wu, Z., Jia, Y., Ma, J., Chen, W., Zhang, L., Yang, J., and Liu, Y. (2019). Strong tribocatalytic dye decomposition through utilizing triboelectric energy of barium strontium titanate nanoparticles. Nano Energy *63*, 103832.

Lin, H., Wu, Z., Jia, Y., Li, W., Zheng, R.-K., and Luo, H. (2014). Piezoelectrically induced mechano-catalytic effect for degradation of dye wastewater through vibrating $Pb(Zr_{0.52}Ti_{0.48})O_3$ fibers. Appl. Phys. Lett. *104*, 162907.

Lin, J.-H., Tsao, Y.-H., Wu, M.-H., Chou, T.-M., Lin, Z.-H., and Wu, J.M. (2017). Single- and few-layers MoS_2nanocomposite as piezo-catalyst in dark and self-powered active sensor. Nano Energy *31*, 575–581.

Liu, Y.-L., and Wu, J.M. (2019). Synergistically catalytic activities of $BiFeO_3/TiO_2$ core-shell nanocomposites for degradation of organic dye molecule through piezophototronic effect. Nano Energy *56*, 74–81.

Liu, Y., Wang, X., Qiao, Y., Min, M., Wang, L., Shan, H., Ma, Y., Hao, W., Tao, P., Shang, W., et al. (2019). Pyroelectricsynthesis of metal–$BaTiO_3$hybrid nanoparticles with enhanced pyrocatalytic performance. ACS Sustain. Chem. Eng. *7*, 2602–2609.

Ma, J., Ren, J., Jia, Y., Wu, Z., Chen, L., Haugen, N.O., Huang, H., and Liu, Y. (2019). High efficiency bi-harvesting light/vibration energy using piezoelectric zinc oxide nanorods for dye decomposition. Nano Energy *62*, 376–383.

Matthias, B.T., and Remeika, J.P. (1951). Dielectric properties of sodium and potassium niobates. Phys. Rev. *82*, 727–729.

Mbarki, R., Haskins, J.B., Kinaci, A., and Cagin, T. (2014). Temperature dependence of flexoelectricity in $BaTiO_3$ and $SrTiO_3$perovskite nanostructures. Phys. Lett. A *378*, 2181–2183.

Miclea, C., Amarande, L., Miclea, C.F., Cioangher, M., Trupina, L., Miclea, C.T., and David, C. (2007). Effect of temperature on the main piezoelectric parameters of Asoft PZT ceramic. Rom. J. Inf. Sci. Technol. *10*, 243–250.

Min, M., Liu, Y., Song, C., Zhao, D., Wang, X., Qiao, Y., Feng, R., Hao, W., Tao, P., Shang, W., et al. (2018). Photothermally enabled pyro-catalysis of a $BaTiO_3$nanoparticle composite membrane at the liquid/air interface. ACS Appl. Mater. Interfaces *10*, 21246–21253.

Morris, M.R., Pendlebury, S.R., Hong, J., Dunn, S., and Durrant, J.R. (2016). Effect of internal electric fields on charge carrier dynamics in a ferroelectric material for solar energy conversion. Adv. Mater. *28*, 7123–7128.

Mushtaq, F., Chen, X., Hoop, M., Torlakcik, H., Pellicer, E., Sort, J., Gattinoni, C., Nelson, B.J., and Pan, S. (2018). Piezoelectrically enhanced photocatalysis with BiFeO3 nanostructures for efficient water remediation. iScience *4*, 236–246.

Mushtaq, F., Chen, X., Staufert, S., Torlakcik, H., Wang, X., Hoop, M., Gerber, A., Li, X., Cai, J., Nelson, B.J., and Pan, S. (2019). On-the-fly catalytic degradation of organic pollutants using magneto-photoresponsive bacteria-templatedmicrocleaners. J. Mater. Chem. A *7*, 24847–24856.

Pan, M., Zhang, C., Wang, J., Chew, J.W., Gao, G., and Pan, B. (2019). Multifunctional piezoelectric heterostructure of $BaTiO_3$@Graphene: decomplexation of Cu-EDTA and recovery of Cu. Environ. Sci. Technol. *53*, 8342–8351.

Penconi, M., Rossi, F., Ortica, F., Elisei, F., and Gentili, P.L. (2015). Hydrogen production from water by photolysis, sonolysis and sonophotolysis with solid solutions of rare earth, gallium and indium oxides as heterogeneous catalysts. Sustainability *7*, 9310–9325.

Pradeep, D., Kumar, A., and Naithani, U.C. (2010). Dependence of specific heat on electric field in $Ba1_{-x}Ca_xTiO_3$ ferroelectric perovskites. Indian J. Pure Appl. Phys. *47*, 43–48.

Qian, W., Wu, Z., Jia, Y., Hong, Y., Xu, X., You, H., Zheng, Y., and Xia, Y. (2017). Thermo-electrochemical coupling for room temperature thermocatalysis in pyroelectricZnOnanorods. Electrochem.Commun. *81*, 124–127.

Rashwan, S.S., Dincer, I., Mohany, A., and Pollet, B.G. (2019). The Sono-Hydro-Gen process (Ultrasound induced hydrogen production): challenges and opportunities. Int. J. Hydrogen Energy *44*, 14500–14526.

Starr, M.B., and Wang, X. (2013). Fundamental analysis of piezocatalysis process on the surfaces

of strained piezoelectric materials. Sci. Rep. *3*, 2160.

Starr, M.B., and Wang, X. (2015). Coupling of piezoelectric effect with electrochemical processes. Nano Energy *14*, 296–311.

Starr, M.B., Shi, J., and Wang, X. (2012). Piezopotential-driven redox reactions at the surface of piezoelectric materials. Angew. Chem. Int. Ed. *51*, 5962–5966.

Su, Y., Zhang, L., Wang, W., Li, X., Zhang, Y., and Shao, D. (2018). Enhanced H2 evolution based on ultrasound-assisted piezo-catalysis of modified MoS_2. J. Mater. Chem. A *6*, 11909–11915.

Suslick, K.S. (1990). Sonochemistry. Science *247*, 1439–1445.

Tan, C.F., Ong, W.L., and Ho, G.W. (2015). Self-biased hybrid piezoelectric-photoelectrochemicalcell with photocatalyticfunctionalities. ACS Nano *9*, 7661–7670.

Tang, Z., Zhao, P., Ni, D., Liu, Y., Zhang, M., Wang, H., Zhang, H., Gao, H., Yao, Z., and Bu, W. (2018). Pyroelectricnanoplatform for NIR-II-triggered photothermal therapy with simultaneous pyroelectric dynamic therapy. Mater. Horizons *5*, 946–952.

Wang, Y.-C., and Wu, J.M. (2020). Effect of controlled oxygen vacancy on H_2-production through the piezocatalysis and piezophototronics of ferroelectric R3C $ZnSnO_3$ nanowires. Adv. Funct. Mater. *30*, 1907619.

Wang, Y., Zhao, D., Ji, H., Liu, G., Chen, C., Ma, W., Zhu, H., and Zhao, J. (2010). Sonochemical hydrogen production efficiently catalyzed by Au/TiO2. J. Phys. Chem. C *114*, 17728–17733.

Wang, S., Wu, Z., Chen, J., Ma, J., Ying, J., Cui, S., Yu, S., Hu, Y., Zhao, J., and Jia, Y. (2019). Lead-free sodium niobate nanowires with strong piezo-catalysis for dye wastewater degradation. Ceramics Int. *45*, 11703–11708.

Whatmore, R. (2017). Ferroelectric materials. In Springer Handbook of Electronic and Photonic Materials, S. Kasap and P. Capper, eds. (Springer Handbooks.Springer), pp. 589–614.

Wu, J. (2018). Advances in Lead-free Piezoelectric Materials (Springer Singapore).

Wu, J., Mao, W., Wu, Z., Xu, X., You, H., Xue, A.X., and Jia, Y. (2016a). Strong pyro-catalysis of pyroelectric $BiFeO_3$ nanoparticles under a room-temperature cold–hot alternation. Nanoscale *8*, 7343–7350.

Wu, J.M., Chang, W.E., Chang, Y.T., and Chang, C.-K. (2016b). Piezo-catalytic effect on the enhancement of the ultra-high degradation activity in the dark by single- and few-layers MoS_2nanoflowers. Adv. Mater. *28*, 3718–3725.

Wu, M.-H., Lee, J.-T., Chung, Y.J., Srinivaas, M., and Wu, J.-M. (2017). Ultrahigh efficient degradation activity of single- and few-layered $MoSe_2$nanoflowers in dark by piezo-catalyst effect. Nano Energy *40*, 369–375.

Wu, J., Qin, N., and Bao, D. (2018a). Effective enhancement of piezocatalytic activity of $BaTiO_3$ nanowires under ultrasonic vibration. Nano Energy *45*, 44–51.

Wu, J., Qin, N., Yuan, B., Lin, E., and Bao, D. (2018b). Enhanced pyroelectric catalysis of $BaTiO_3$ nanowires for utilizing waste heat in pollution treatment. ACS Appl. Mater. Interfaces *10*, 37963–37973.

Wu, J.M., Sun, Y.-G., Chang, W.-E., and Lee, J.-T. (2018c). Piezoelectricity induced water splitting and formation of hydroxyl radical from active edge sites of MoS_2nanoflowers. Nano Energy *46*, 372–382.

Xia, B., Guo, Q., Gao, D., Shi, S., and Tao, K. (2016). High temperature ferromagnetism in Cu-doped MoS_2nanosheets. J. Phys. D: Appl. Phys. *49*, 165003.

Xia, Y., Jia, Y., Qian, W., Xu, X., Wu, Z., Han, Z., Hong, Y., You, H., Ismail, M., Bai, G., and Wang, L. (2017). Pyroelectrically induced pyro-electro-chemical catalytic activity of $BaTiO_3$nanofibers under room-temperature cold–hot cycle excitations. Metals *7*, 1–9.

Xiang, C., Papadantonakis, K.M., and Lewis, N.S. (2016). Principles and implementations of electrolysis systems for water splitting. Mater. Horizons *3*, 169–173.

Xie, M., Dunn, S., Boulbar, E.L., and Bowen, C.R. (2017). Pyroelectric energy harvesting for water splitting. Int. J. Hydrogen Energy *42*, 23437–23445.

Xu, X., Chen, S., Wu, Z., Jia, Y., Xiao, L., and Liu, Y. (2018a). Strong pyro-electro-chemical coupling of $Ba_{0.7}Sr_{0.3}TiO_3$@Ag pyroelectric nanoparticles for room-temperature pyrocatalysis. Nano Energy *50*, 581–588.

Xu, W.W., Tzanakis, I., Srirangam, P., Terzi, S., Mirihanage, W.U., Eskin, D.G., Mathiesen, R.H., Horsfield, A.P., and Lee, P.D. (2015). In Situ Synchrotron Radiography of Ultrasound Cavitation in a Molten Al-10Cu Alloy. TMS2015 Supplemental. Proceedings, 61–66.

Xu, X., Xiao, L., Jia, Y., Wu, Z., Wang, F., Wang, Y., Haugen, N.O., and Huang, H. (2018b). Pyro-catalytic hydrogen evolution by $Ba_{0.7}Sr_{0.3}TiO_3$ nanoparticles: harvesting cold–hot alternation energy near room-temperature. Energy Environ. Sci. *11*, 2198–2207.

Xue, X., Zang, W., Deng, P., Wang, Q., Xing, L., Zhang, Y., and Wang, Z.L. (2015). Piezo-potential enhanced photocatalytic degradation of organic dye using ZnO nanowires. Nano Energy *13*, 414–422.

You, H., Jia, Y., Wu, Z., Wang, F., Huang, H., and Wang, Y. (2018a). Room-temperature pyro-catalytic hydrogen generation of 2D few-layer black phosphorene under cold-hot alternation. Nat. Commun. *9*, 2889.

You, H., Ma, X., Wu, Z., Fei, L., Chen, X., Yang, J., Liu, Y., Jia, Y., Li, H., Wang, F., and Huang, H. (2018b). Piezoelectrically/pyroelectrically-driven vibration/cold-hot energy harvesting for mechano-/pyro- bi-catalytic dye decomposition of $NaNbO_3$nanofibers. Nano Energy *52*, 351–359.

You, H., Wu, Z., Zhang, L., Ying, Y., Liu, Y., Fei, L., Chen, X., Jia, Y., Wang, Y., Wang, F., et al. (2019). Harvesting the vibration energy of $BiFeO_3$nanosheets for hydrogen evolution. Angew. Chem. Int. Ed. *58*, 11779–11784.

Zhang, J., Yao, K.L., Liu, Z.L., Gao, G.Y., Sun, Z.Y., and Fan, S.W. (2010). First-principles study of the ferroelectric and nonlinear optical properties of the $LiNbO_3$-type $ZnSnO_3$. Phys. Chem. Chem. Phys. *12*, 9197–9204.

Zhang, H., Zhang, S., Yao, G., Huang, Z., Xie, Y., Su, Y., Yang, W., Zheng, C., and Lin, Y. (2015). Simultaneously harvesting thermal and mechanical energies based on flexible hybrid nanogenerator for self-powered cathodicprotection. ACS Appl. Mater. Interfaces *7*, 28142–28147.

Zhang, Y., Xie, M., Adamaki, V., Khanbareh, H., and Bowen, C.R. (2017). Control of electro-chemical processes using energy harvesting materials and devices. Chem. Soc. Rev. *46*, 7757–7786.

Zhang, Y., Kumar, S., Marken, F., Krasny, M., Roake, E., Eslava, S., Dunn, S., Da Como, E., and Bowen, C.R. (2019). Pyro-electrolytic water splitting for hydrogen generation. Nano Energy *58*, 183–191.

Zhang, Y., Phuong, P.T.T., Roake, E., Khanbareh, H., Wang, Y., Dunn, S., and Bowen, C. (2020). Thermal energy harvesting using pyroelectric-electrochemical coupling in ferroelectric materials. Joule *4*, 301–309.

Zheng, T., Wu, J., Xiao, D., and Zhu, J. (2018). Recent development in lead-free perovskite piezoelectric bulk materials. Prog.Mater. Sci. *98*, 552–624.

Zhou, M., Yang, H., Xian, T., Li, R.S., Zhang, H.M., and Wang, X.X. (2015). Sonocatalytic degradation of RhB over $LuFeO_3$ particles under ultrasonic irradiation. J. Hazard. Mater. *289*, 149–157.

Zhu, L., Gao, M., Peh, C.K.N., and Ho, G.W. (2018). Solar-driven photothermal nanostructured materials designs and prerequisites for evaporation and catalysis applications. Mater. Horizons *5*, 323–343.

iScience, Volume *23*

Supplemental Information

Demonstration of Enhanced Piezo-Catalysis for Hydrogen Generation and Water Treatment at the Ferroelectric Curie Temperature

Pham Thi, Thuy Phuong, Yan, Zhang, Nick, Gathercole, Hamideh, Khanbareh, Nguyen Phuc, Hoang Duy, Xuefan, Zhou, Dou, Zhang, Kechao, Zhou, Steve, Dunn, and Chris, Bowen

Supporting Information

Transparent Methods

Material preparation:

$Ba_{0.75}Sr_{0.25}TiO_3$ (BST) powders were prepared by a solid-state reaction. Analytical grade (Sigma Aldrich) barium carbonate ($BaCO_3$, 99%), strontium carbonate ($SrCO_3$, 99%), and titanium dioxide (TiO_2, 99.9%) were selected as starting materials and weighed according to their stoichiometric ratio. The above mixtures were calcined at 1200 °C for 3 h, followed by additional ball-milling for 24 h. The milled powders were mixed with 1 wt.% poly(vinyl alcohol) (PVA) binder and dried in an oven at 60 °C. To form dense materials for characterisation, the powders were uni-axially cold-compacted to form pellets of 10 mm in diameter and 1 mm in thickness. The pellets were first heated to 500 °C for 3h to remove the binder and then sintered at 1325 °C for 4 h.

Characterization:

The phase structure of the BST powders was examined by X-ray diffractometer (BRUKER D8-Advance, USA) with Cu radiation with 2θ ranging from 20°-70°. The morphology of the BST powders was examined by a scanning electron microscopy (SEM, JSM6480LV, Tokyo, Japan). For electro-physical measurements of sintered materials, silver paint was coated on both working faces of the sintered samples to form electrodes. The temperature dependence of the dielectric constant (relative permittivity) and polarization of the unpoled pellets were studied in a temperature range of 26-67 °C using an impedance analyzer (Solartron 1260, Hampshire, UK) at a frequency of 1 kHz and a Radiant RT66B-HVi Ferroelectric Test system at hysteresis period of 10 ms, respectively. Piezo force microscopy (PFM) in contact mode of an atomic force microscope (NanoManTM VS) with a conductive Pt/Ir-coated Si cantilever (SCM-PIT) was used to investigate the piezo-response phase and amplitude of BST sample. The ceramic sample was polished, thermally etched, and ground to 0.2 mm before measurement. A direct current (DC)

voltage from -10 to 10V was applied superimposed on an AC modulation voltage during polarisation switching.

Hydrogen production experiments:

A mass of 1 mg of BST powder was added and dispersed into a 20 mL headspace vial containing 10 mL of distilled water and methanol (Merk) mixture. After sealing tightly, it was placed in the center of an ultrasonic cleaner bath (60W-TP01-Taiwan Total Meter) and purged with argon for 15 min to completely remove air prior to being sonicated for a desired reaction time at a frequency of 40 kHz (see **Figure S2**). For online measurement, the generated hydrogen was continuously swept by argon stream at about 12 ml/min and passed to a 120 mL-condensation bottle before sending to a gas chromatograph (HP 5890 Series II, Agilent) equipped with a thermal conductivity detector and RT-Msieve 13X capillary column (30 m x 0.32 mm, Thames Restek) by ChemStation Software (see Figure S3). Actual flow rates were verified with a soap-film bubble flowmeter (Hewlett-Packard) prior to each run. The hydrogen production rate was calculated using a calibration curve that was made by using different concentrations of hydrogen diluted in argon. During the experiment, the ultrasonic bath temperature was controlled by circulating cooled water back to the ultrasonic bath. The *control* (non-ferroelectric particulate addition) tests were performed at the same conditions with 1 mg of α-Al_2O_3 (Merk) as an inert material and *blank* tests without adding any solid particle to the reaction mixture. This allowed the *sono-chemical* contribution to hydrogen generation be determined. The uncertainties have been estimated by at least three experiments. The *piezo-catalytic* hydrogen generation was calculated by simple subtraction of hydrogen evolution rates obtained from experiments with BST and blank tests due to no statistical difference in hydrogen generated from control and blank tests, then divided by the amount of BST.

Rhodamine B degradation experiments:

A mass of 2 mg of BST powder was added and dispersed into a 20 mL headspace vial containing 10 mL of RhB solution (10 mg/L), which has been widely chosen as a model contaminant based on its popularity among research groups (Rochkind et al., 2015). By conducting mutually exclusive experiments without

applying ultrasound, it was found that the direct photolytic degradation, adsorption and thermal degradation of RhB on BST are negligible. Thus, all further experiments were performed at normal light condition and without adsorption pre-treatment. The absorption spectra of the treated samples were acquired with a UV-Vis spectrophotometer.

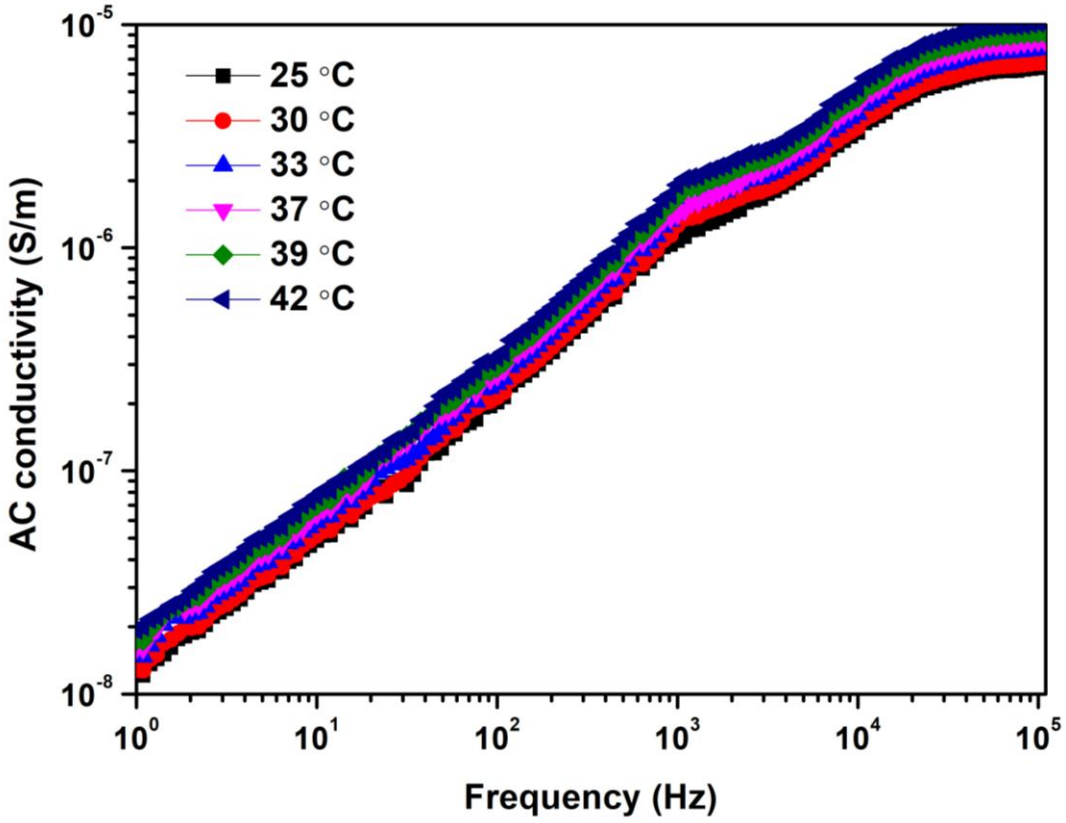

Figure S1 AC conductivity of BST with different frequencies and temperatures, related to Figure 1.

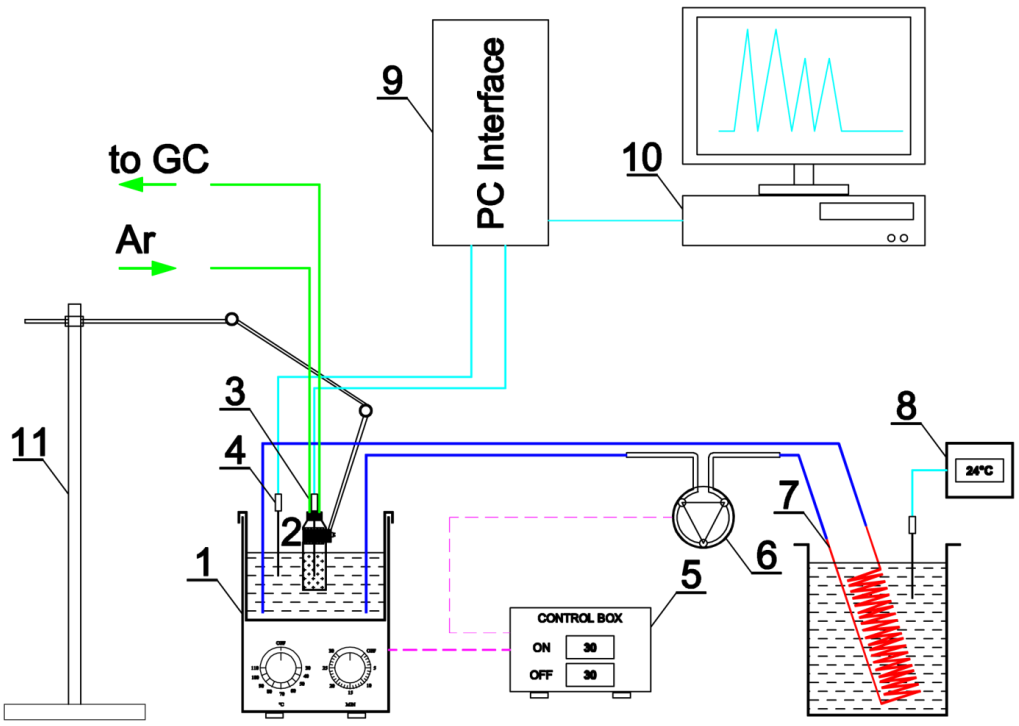

Figure S2. Schematic image of the experimental setup. 1 – Ultrasonic bath; 2 – Sample vial; 3 – Inside temperature sensor; 4 – Water bath temperature sensor; 5 – Timers; 6 – Peristaltic pump; 7 – Cooling coil; 8 – Cooling bath temperature sensor; 9 – Interface; 10 – Computer; 11 – Flexible stand, related to Figure 2.

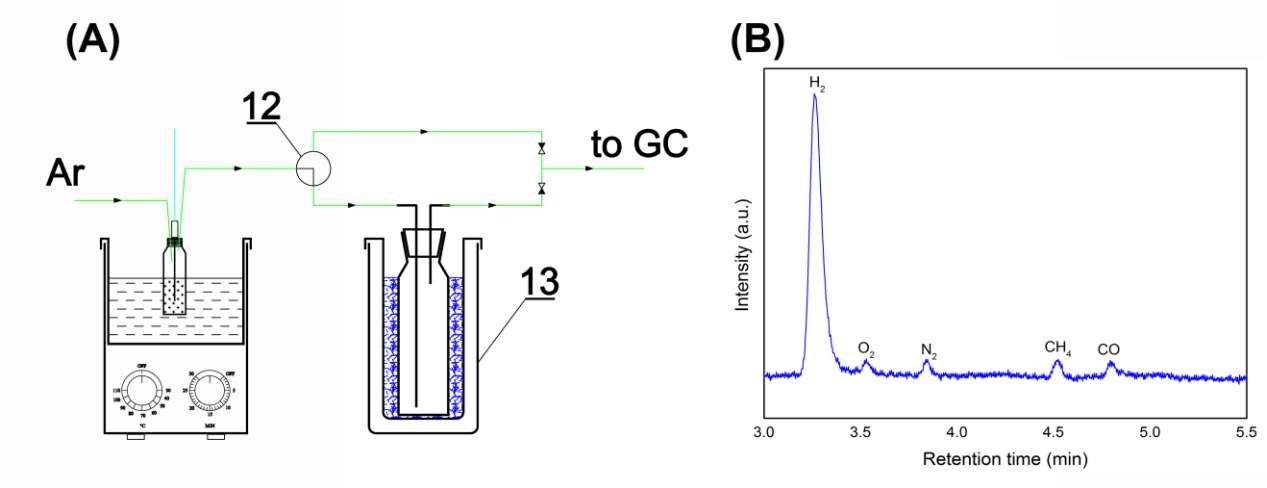

Figure S3. (A) Online hydrogen measurement setup. (B) Representative GC-TCD chromatogram of the produced sample at optimum conditions. 12 – Three ways valve; 13 – Condensation bottle, related to Figure 2.

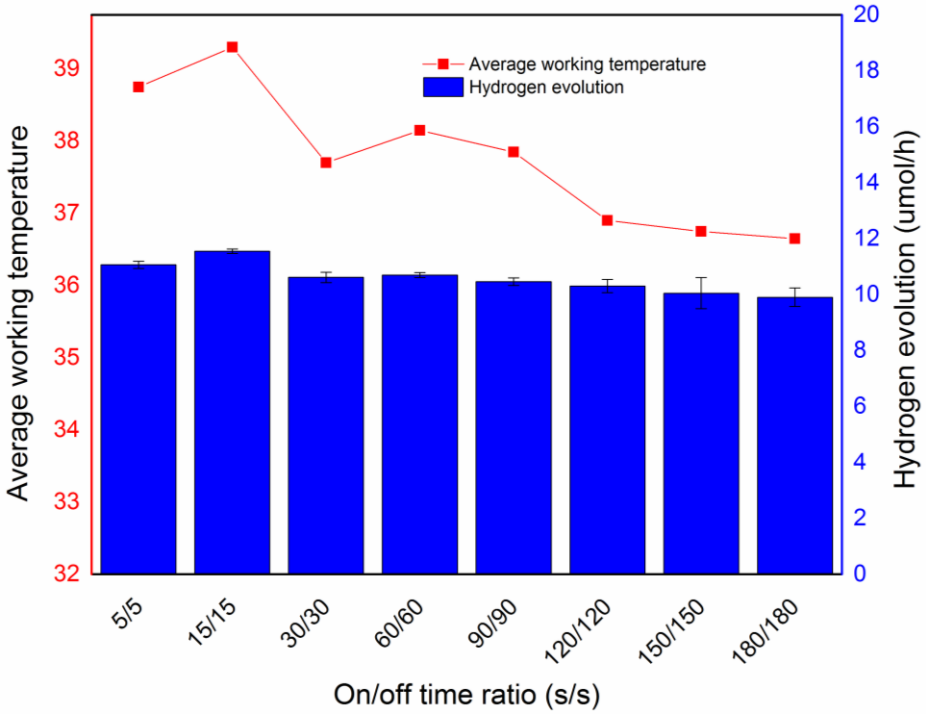

Figure S4. Hydrogen generation for blank test, with sono-chemcial produced hydrogen shown to be temperature independent, related to Figure 2.

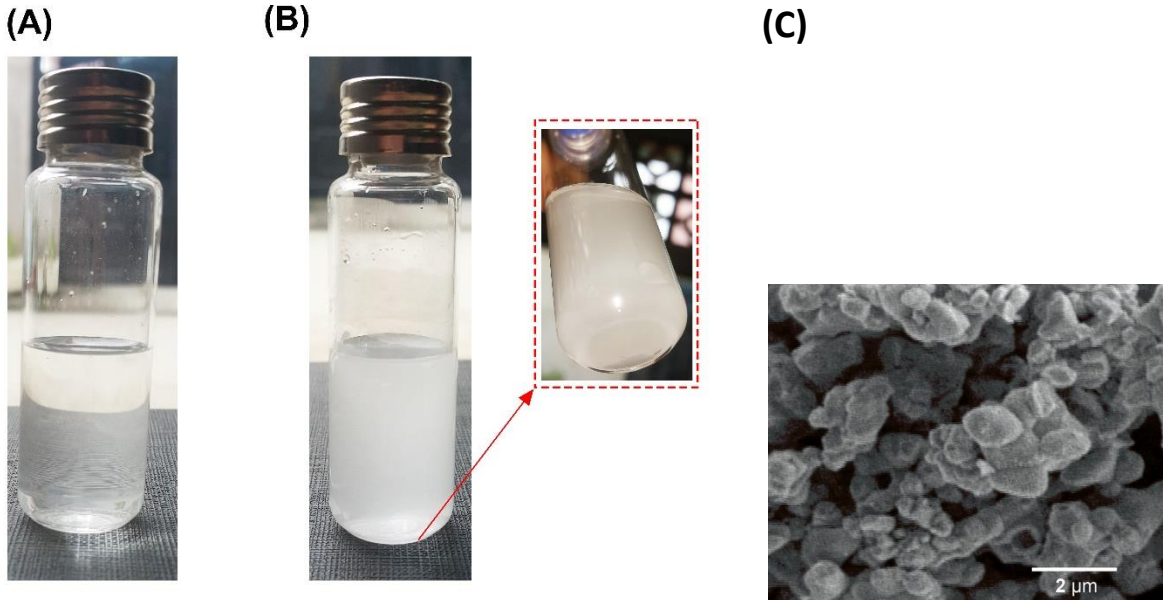

Figure S5. Images of the aqueous solution before and after powder addition. (A) pure water, (B) BST aqueous suspension after the application of ultrasound excitation, inset shows no precipitation can be seen on the bottom side, (C) SEM image of the BST powder after the application of ultrasound, related to Figure 2.

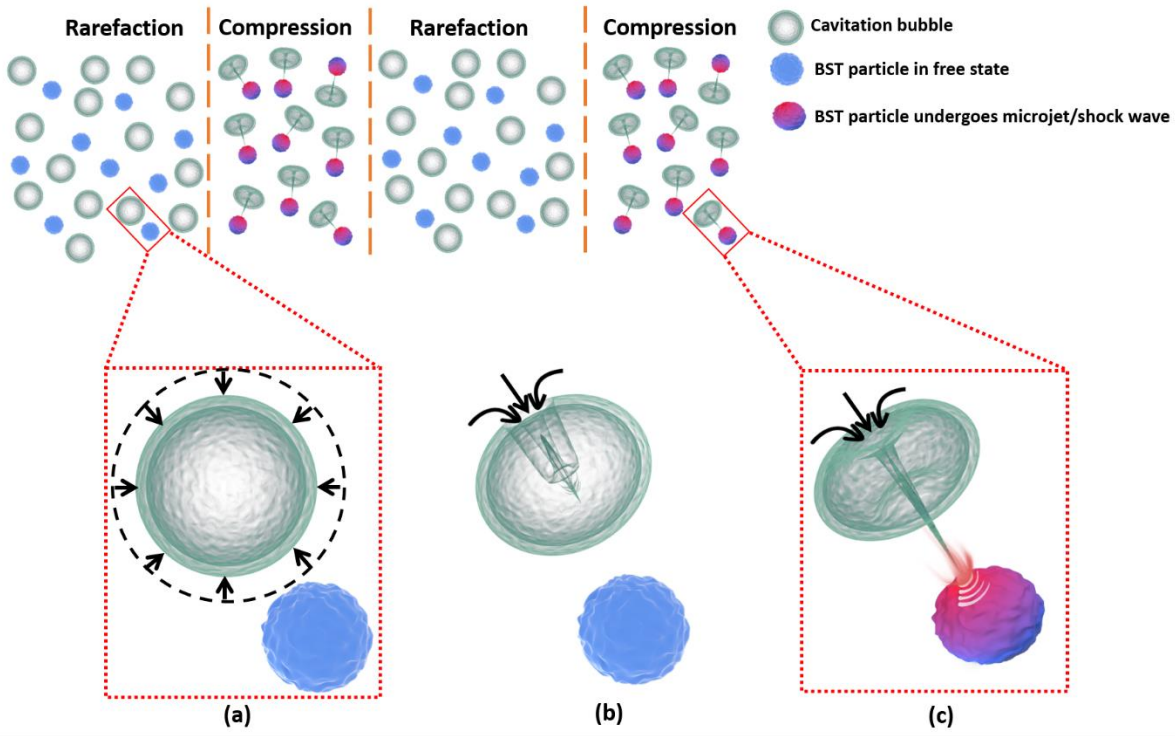

Figure S6. Schematic of ultrasound applied to ferroelectric particle, related to Figure 3.

Table S1 Rate of hydrogen evolution under different conditions, , related to Figure 4.

Effect	Material	**Hydrogen evolution rate**		**Reference**
		μmol/h	mmol/h/g	
Pyro-catalytic	BST	n/a	0.0078 [a]	(Xu et al., 2018)
Sono-chemical		3.4 [b]	n/a	(Wang et al., 2010)
		10.83 ± 0.13 [c]	n/a	This work
Sono-catalytic	*Au/TiO_2*	282.3 [b]	3.8 [b]	(Wang et al., 2010)
Piezo-photo-catalytic	$KNbO_3/MoS_2$	n/a	0.096 [d]	(Jia et al., 2019)
Sono-piezo-catalytic	BST	14.42 ± 0.15 [c]	14.42 ± 0.15 [c]	This work
	$ZnSnO_3$	n/a	3.5 [e]	(Wang and Wu, 2019)
	MoS_2	n/a	0.028 [f]	(Su et al., 2018)
	$BiFeO_3$	n/a	0.026 [g]	(You et al., 2019)
Extracted piezo-catalytic effect	BST	3.59 [c]	3.59 [c]	This work

n/a abbreviates either not available or not applicable

[a] Thermal cycle is 10 min with thermal fluctuation of 25-50 °C, concentration of methanol is 20 vol%

[b] Concentration of methanol was 4 vol%, ultrasound source of 40kHz at 50 W

[c] Concentration of methanol was 4 vol%, ultrasound source of 40kHz at 60 W, ultrasound on/off time ratio is 15/15s with thermal fluctuation of 40.5 - 42 °C

[d] Triethanolamine was used as a sacrificial reagent (15%), ultrasound source of 40kHz at 110 W

[e] Anhydrous alcohol was used as a sacrificial reagent (50 vol%), ultrasound source of 40kHz at 250 W

[f] Fe2+ was used as inorganic oxidizable sacrificial agent, ultrasound source of 40kHz at 140 W

[g] Na_2SO_3 was used as a sacrificial reagent (0.05M), ultrasound source of 45kHz at 50 W

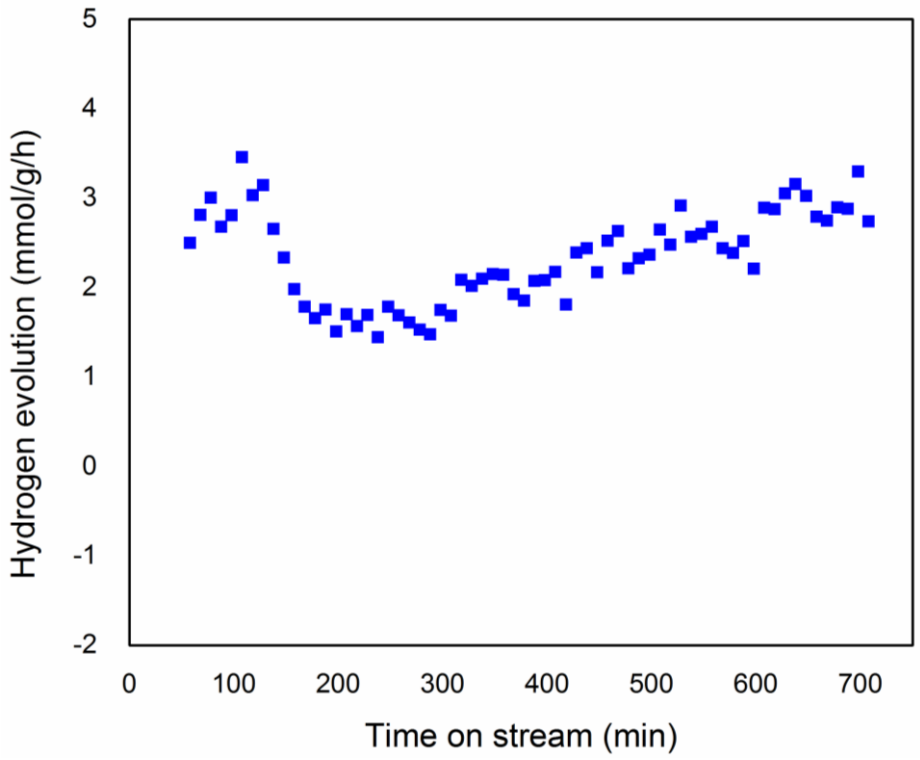

Figure S7. Piezo-catalytic hydrogen generation with time on stream, related to Figure 4.

In this experiment, a condensable bottle (see Fig. S2-A) was used to determine a stable hydrogen production rate. Thus, there is a spike at ~100 mins which is the required duration time for the H_2 to fully fill the bottle. H_2 production was found to be affected by methanol concentration, therefore a subsequent decrease (200min) may be a result of a decrease in methanol concentration due to its vaporisation. At long times, >200min the sample volume is likely to decrease during ultrasound excitation, resulting an increase in inside temperature (outside temperature and ultrasound power were constant), thus, an increase of H_2 production rate may occur for longer durations.

Reference

JIA, S., SU, Y., ZHANG, B.-P., ZHAO, Z., LI, S., ZHANG, Y., LI, P., XU, M. & REN, R. 2019. Few-Layer MoS_2 Nanosheet-Coated $KNbO_3$ Nanowire Heterostructures: Piezo-Photocatalytic Effect Enhanced Hydrogen Production and Organic Pollutant Degradation. *Nanoscale*.

ROCHKIND, M., PASTERNAK, S. & PAZ, Y. 2015. Using Dyes for Evaluating Photocatalytic Properties: A Critical Review. *Molecules,* 20**,** 88-110.

SU, Y., ZHANG, L., WANG, W., LI, X., ZHANG, Y. & SHAO, D. 2018. Enhanced H_2 evolution based on ultrasound-assisted piezo-catalysis of modified MoS_2. *Journal of Materials Chemistry A,* 6**,** 11909-11915.

WANG, Y.-C. & WU, J. M. 2019. Effect of Controlled Oxygen Vacancy on H2-Production through the Piezocatalysis and Piezophototronics of Ferroelectric R3C $ZnSnO_3$ Nanowires. *Advanced Functional Materials,* n/a**,** 1907619.

WANG, Y., ZHAO, D., JI, H., LIU, G., CHEN, C., MA, W., ZHU, H. & ZHAO, J. 2010. Sonochemical Hydrogen Production Efficiently Catalyzed by Au/TiO_2. *The Journal of Physical Chemistry C,* 114**,** 17728-17733.

XU, X., XIAO, L., JIA, Y., WU, Z., WANG, F., WANG, Y., HAUGEN, N. O. & HUANG, H. 2018. Pyro-catalytic hydrogen evolution by $Ba_{0.7}Sr_{0.3}TiO_3$ nanoparticles: harvesting cold–hot alternation energy near room-temperature. *Energy & Environmental Science,* 11**,** 2198-2207.

YOU, H., WU, Z., ZHANG, L., YING, Y., LIU, Y., FEI, L., CHEN, X., JIA, Y., WANG, Y., WANG, F., JU, S., QIAO, J., LAM, C.-H. & HUANG, H. 2019. Harvesting the Vibration Energy of $BiFeO_3$ Nanosheets for Hydrogen Evolution. *Angewandte Chemie International Edition,* 58**,** 11779-11784.